This is an open access article published under a Creative Commons Non-Commercial No Derivative Works (CC-BY-NC-ND) Attribution License, which permits copying and redistribution of the article, and creation of adaptations, all for non-commercial purposes.

NANO LETTERS

Letter

Cite This: Nano Lett. 2017, 17, 6511-6515

pubs.acs.org/NanoLett

Observation of Conductance Quantization in InSb Nanowire Networks

Elham M. T. Fadaly,[†,‡] Hao Zhang,[*,†] Sonia Conesa-Boj,[†] Diana Car,[†,‡] Önder Gül,[†] Sébastien R. Plissard,[‡] Roy L. M. Op het Veld,[†,‡] Sebastian Kölling,[‡] Leo P. Kouwenhoven,[†,§] and Erik P. A. M. Bakkers[*,†,‡]

[†]QuTech and Kavli Institute of Nanoscience, Delft University of Technology, 2600 GA Delft, The Netherlands

[‡]Department of Applied Physics, Eindhoven University of Technology, 5600 MB Eindhoven, The Netherlands

[§]Microsoft Station Q Delft, 2600 GA Delft, The Netherlands

Supporting Information

ABSTRACT: Majorana zero modes (MZMs) are prime candidates for robust topological quantum bits, holding a great promise for quantum computing. Semiconducting nanowires with strong spin orbit coupling offer a promising platform to harness one-dimensional electron transport for Majorana physics. Demonstrating the topological nature of MZMs relies on braiding, accomplished by moving MZMs around each other in a certain sequence. Most of the proposed Majorana braiding circuits require nanowire networks with minimal disorder. Here, the electronic transport across a junction between two merged InSb nanowires is studied to investigate how disordered these nanowire networks are. Conductance quantization plateaus are observed in most of the contact pairs of the epitaxial InSb nanowire networks: the hallmark of ballistic transport behavior.

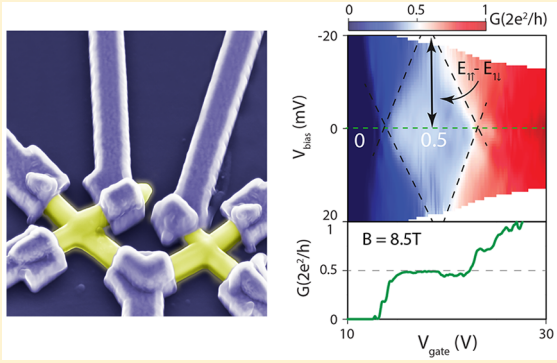

KEYWORDS: *Semiconducting nanowires, networks, indium antimonide, conductance quantization, ballistic transport*

Semiconductor nanowires (NWs) with strong spin−orbit coupling, for example, InSb or InAs, provide a promising platform to study Majorana-related physics. Majorana zero modes (MZMs) are predicted to appear in carefully engineered solid state systems, which can be utilized as building blocks for the topological quantum computer by using their nonabelian properties.[1−3] When a 1D semiconductor with low disorder and strong spin−orbit interaction (SOI) is brought into contact with a superconductor under an external magnetic field, MZMs appear at both ends of the proximitized semiconductor region.[4,5] Signatures of MZMs have been experimentally observed in InSb and InAs semiconductor/superconductor hybrid NW systems.[6−14] The ambitious goal of performing logical operations utilizing Majoranas and studying their non-Abelian properties, that is, braiding, requires NW networks. These networks are required to move MZMs around each other or to tune the coupling between each other in a certain sequence, according to most of the theoretical proposals.[15−19] The semiconductor NW network system of our preference is InSb since it exhibits a higher electron mobility,[20] stronger SOI,[21] and larger Landé *g*-factor than InAs.[22−25]

High structural quality InSb NW networks have been recently reported by Car et al.[26] To date, several transport experiments have been performed on branched NW networks.[27−31] However, one remaining unanswered question is the degree of disorder in this system. Disorder is a serious issue as it can mimic Majorana signatures or even can be completely detrimental to the topological protection of MZMs.[9] In InSb NW devices, disorder has been diminished to the point where ballistic transport, whose hallmark is quantized conductance plateaus, is observed.[25,32] A recent work has been published showing ballistic transport in the straight channels in InAs NW networks, mimicking single NWs.[31] Yet, ballistic transport across the junction in NW networks, especially in InSb NWs, has not been reported yet.

Here, we study the electronic transport across the junction between two merged InSb NWs using the optimized nanofabrication recipe reported in refs 9 and 25. In this work, the evolution of the quantized conductance plateaus in each contact pair is studied as a function of magnetic field, gate voltage, and source−drain bias voltage. Quantized conductance plateaus are observed consistently in most of the contact pairs of the epitaxially grown InSb NW networks in three different devices. The Landé-*g* factor of the first subband is extracted for each contact pair in the NW network. Additionally, the structural quality of the junction between the crossed NWs in a representative device has been inspected by cross-sectional transmission electron microscopy (XTEM) and correlated with the transport measurements.

The InSb NW networks used in this work have been synthesized by gold (Au) catalyzed vapor−liquid−solid (VLS)

Received: February 23, 2017
Revised: June 30, 2017
Published: June 30, 2017

 © 2017 American Chemical Society

DOI: 10.1021/acs.nanolett.7b00797
Nano Lett. 2017, 17, 6511−6515

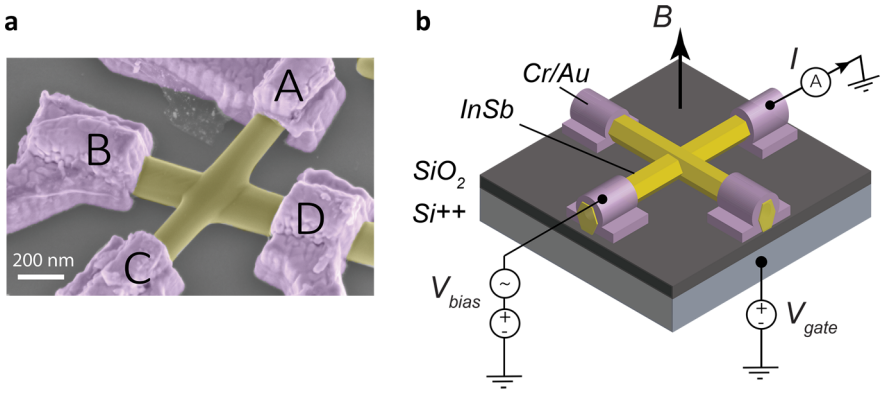

Figure 1. A typical InSb NW cross device. (a) A false-colored, 30°-tilted SEM image of an InSb NW cross (yellow) deposited on a p++-doped Si substrate (light gray) covered with 285 nm of SiO_2 (dark gray) and contacted with 10/210 nm of Cr/Au (purple). The NW network terminals are labeled A, B, C, and D. (b) Schematic illustration of the experimental setup. The Si substrate acts as a global back gate, and the SiO_2 is the gate dielectric. A gate voltage (V_{gate}) is applied to the Si substrate. A source−drain voltage bias (V_{bias}) is applied between two terminals of the NW network, and the current is monitored between these two terminals. The rest of the terminals are floated. All of the measurements are performed at a temperature of 300 mK and an out-of-plane magnetic field.

growth mechanism in a metal−organic vapor phase epitaxy (MOVPE) machine. Kinked InP NWs grown on InP (001) substrate have been used as stems for the growth of InSb ⟨111⟩ B NW networks. Since the InSb NW networks are in an epitaxial relationship to the InP substrate, the crossed InSb NWs meet under an angle of 109.5° which corresponds to the crystallographic angle between two ⟨111⟩ B directions in a zinc blende crystal structure. Further details related to the NW networks growth and the structural quality of these networks have been reported in ref 26. After growth, the NW networks are deterministically transferred from the growth chip via a nanomanipulator in a scanning electron microscope (SEM) to the desired chip for device fabrication as shown in the Supporting Figure S1 and the Supporting Video. Figure 1a shows a false color 30° tilted SEM image of a typical InSb NW network device after the fabrication process. The InSb network is deposited on a P++-doped Si substrate covered with 285 nm of SiO_2. The electrical contacts to the InSb network are defined by electron beam lithography followed by the evaporation of metallic normal contacts (10/210 nm of Cr/Au). Prior to contact deposition, the surface oxide of the InSb network is removed via sulfur passivation and short in situ He-ion milling. Further details of the device fabrication process are explained in the Supporting Text in S1. Afterward, the sample is mounted in a ^{3}He cryostat with a base temperature of 300 mK, single axis magnet of 9 T perpendicular to the substrate and measured using a standard lock-in technique at 73 Hz with an excitation route mean square voltage (V_{RMS}) 30 μV. A back gate voltage (V_{gate}) is applied to the Si substrate, and the SiO_2 acts as a gate dielectric. A bias voltage is applied to one contact, and the current is measured through another grounded contact, while the rest of the contacts are left floating. This setup is the same for each contact pair in the NW network as illustrated schematically in Figure 1b. All data reported below are calibrated after subtracting resistances of the filters and the wiring of the cryostat system. However, we would like to emphasize that no contact resistance is subtracted from the data presented in this work, since we cannot extract the exact value of the contact resistance from the two terminal measurements. This suggests that, in some devices, the conductance value to which a plateau is pinned can be a lower bound of the real conductance value.

Differential conductance is measured using a standard lock-in technique by applying a small ac excitation voltage (V_{ac}) at a fixed dc bias voltage and measuring the ac current (I_{ac}) such that $G = dI_{ac}/dV_{ac}$. The channel length denoted by the contact spacing between the different contact pairs is measured from the top-view SEM image of the device shown in Figure 1a. The lengths of the two straight contact pairs labeled as A−C and B−D are 770 and 640 nm, respectively. The lengths of the kinked contact pairs A−B, A−D, B−C, and D−C are 700, 610, 700, and 700 nm, respectively. In principal, ballistic transport behavior is very challenging to realize in such a NW network with this geometry for the following reasons. The NW system already has a large surface-to-volume ratio which can cause electrons to scatter back to the source reservoir. In addition, the conductance plateau quality greatly depends on the channel length, that is, contact spacing. Our NW network devices have long contact spacing between the contact pairs (∼700 nm) which is much larger than the electrons mean free path reported in single ballistic NW devices (∼150 nm).[25,32,33] Concerning the geometry of the NW network devices, the interface between merged NWs can induce additional scattering. Furthermore, electrons traversing the crossed networks are required to follow a bended trajectory to comply with the device geometry. This is in sharp contrast to the single nanowire case and will cause extra scattering even in a perfectly clean nanowire network system.

Figure 2a−d shows differential conductance ($G = dI/dV_{bias} = I_{AC}/V_{AC}$) of three different contact pairs of the network (A−B, A−C, A−D) as a function of V_{gate} and B at V_{bias} = 0 mV (the data for B−C, B−D, C−D can be found in Figures S5 and S6). For increased clarity, line cuts at different B values, 0 T (green), 5 T (red), and 8 T (black), are shown in the bottom panels with a horizontal offset. At zero magnetic field, no quantized conductance plateaus are observed which is expected due to the many possible scattering sources previously discussed. As the magnetic field is increased, backscattering of electrons is suppressed, and the first spin resolved conductance plateau ($G = e^2/h$) is revealed. It becomes more pronounced and flatter at higher magnetic fields. In some devices (Figure S7), higher plateaus [up to three plateaus (e^2/h, $2e^2/h$, $3e^2/h$)] are observed. In this paper, the focus is on the first plateau which is present in all our devices. The line cuts in the bottom panels of the color plots in Figure 2 exhibit a clear evolution of the first

DOI: 10.1021/acs.nanolett.7b00797
Nano Lett. 2017, 17, 6511−6515

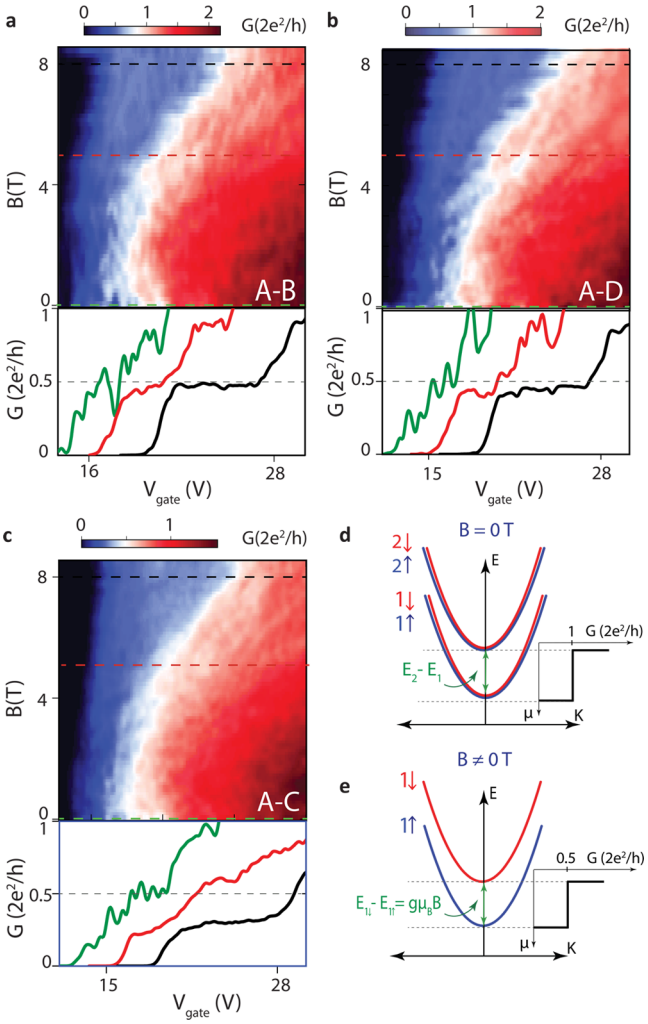

Figure 2. (a–c) Color plots of differential conductance ($G = dI/dV_{bias}$) as a function of V_{gate} and magnetic field B at $V_{bias} = 0$ mV for different contact pair combinations: (a) A–B, (b) A–D, (c) A–C. The bottom panels in a–c show I–V traces indicating line cuts of a–c at different B values 0 T (green), 5 T (red), and 8 T (black) with a horizontal offset between the individual traces for clarity. (d–e) Energy spectra at different B values, sketching the evolution of the spin resolved subbands. In this panel, the energy spectrum near the bottom of the first subband and the corresponding conductance region are shown. (e) In the absence of magnetic field ($B = 0$), the energy spectrum shows the first two-spin degenerate subbands, and the energy spacing between them is denoted as $E_1 - E_2$ where $G = 2e^2/h$. (f) At nonzero magnetic field ($B \neq 0$), the spin-degeneracy is lifted, and the energy spacing between the two lowest spin-split subbands ($E_{1\downarrow}$, $E_{1\uparrow}$) is purely due to Zeeman splitting ($\Delta E_{subband} = E_{1\uparrow} - E_{1\downarrow} = g\mu_B B$). When the chemical potential reaches the lowest spin-split subband, the conductance is e^2/h instead of $2e^2/h$.

quantized plateau toward ($G = e^2/h$) with increasing B confirming that magnetic field helps ballistic transport by suppressing electrons' backscattering. Most of the contact pairs in the NW network shows extended conductance plateaus around e^2/h (without any contact resistance being subtracted from the plots), except for one straight channel (A–C) that exhibits an unexpectedly reduced plateau value (around $0.3 \times 2e^2/h$). Currently the reason for this unexpected low plateau of this particular channel is unclear. The fact that all the other contact pairs involving contact A or C (e.g., A–B, A–D, C–B, C–D) show regular plateau values (around e^2/h) indicates that the low plateau value of the A–C contact pair is not due to poor electrical contacts of A or C.

For further investigations, at $B = 8.5$ T, the differential conductance for different contact pairs in the NW network is measured as a function of V_{gate} and V_{bias} as illustrated in the color plots in Figure 3a–c. The color plots exhibit diamond

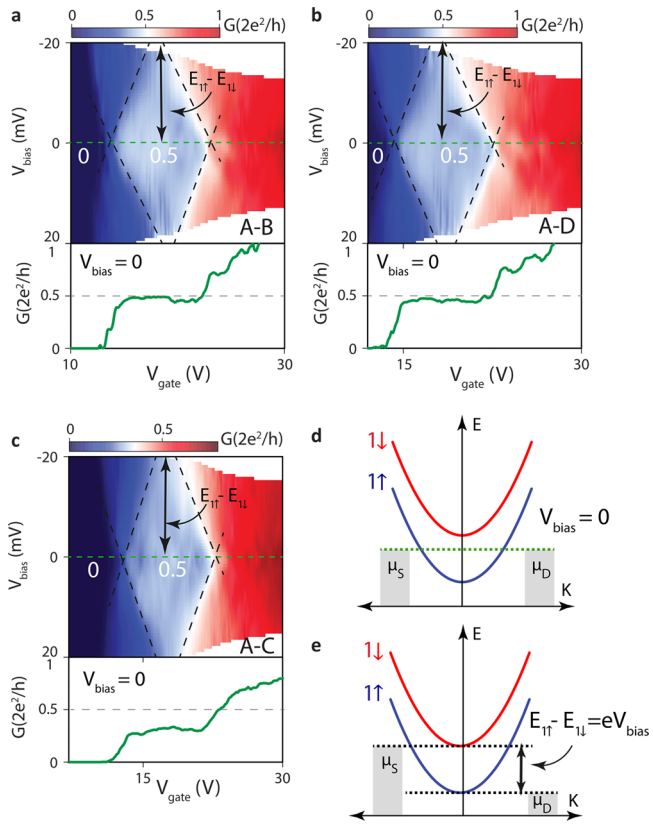

Figure 3. Voltage bias spectroscopy. (a–c) Color plots of the differential conductance $G = dI/dV_{bias}$ as a function of V_{bias} and V_{gate} at $B = 8.5$ T. A line cut along $V_{bias} = 0$ mV (green) is shown in the bottom panel. Black dotted lines surrounding a diamond shaped region, indicating the edge of the first quantized conductance plateau, are drawn as guide to the eye. (d–e) Energy spectra showing the lowest two spin-split subbands such that (d) at $V_{bias} = 0$ mV (along the dotted green line), the source and drain chemical potential (μ_s, μ_d) are aligned together in between $E_{1\uparrow}$ and $E_{1\downarrow}$ and (e) at $V_{bias} \neq 0$ mV, the source and the drain chemical potential (μ_s, μ_d) are aligned to the spin-split subbands $E_{1\downarrow}$ and $E_{1\uparrow}$, respectively. In this case, the subband spacing is equivalent to the bias voltage ($\Delta E_{subband} = E_{1\uparrow} - E_{1\downarrow} = eV_{bias}$).

shaped regions of constant conductance ($G = e^2/h$) highlighted by dotted black lines. Line cuts of these color plots, indicated by the green dotted line, along ($V_{bias} = 0$ mV) are shown in the bottom panels. In the middle of the diamond, at zero bias voltage, a prolonged conductance plateau appears at e^2/h. This can be explained by the energy spectrum shown in Figure 3d where the chemical potentials of the source and drain (μ_s, μ_d) are aligned together between $E_{1\uparrow}$ and $E_{1\downarrow}$. At the tips of the diamond where the dotted lines cross each other, the bias voltage is equivalent to the first spin-split subband spacing ($E_{1\downarrow} - E_{1\uparrow} = eV_{bias}$) enabling the extraction of the subband spacing as illustrated schematically in the energy spectrum in Figure 3e. Accordingly, the Landé g-factor (g_1) of the first channel for each contact pair in the NW network can be extracted since the measured subband spacing is purely due to Zeeman

DOI: 10.1021/acs.nanolett.7b00797
Nano Lett. 2017, 17, 6511–6515

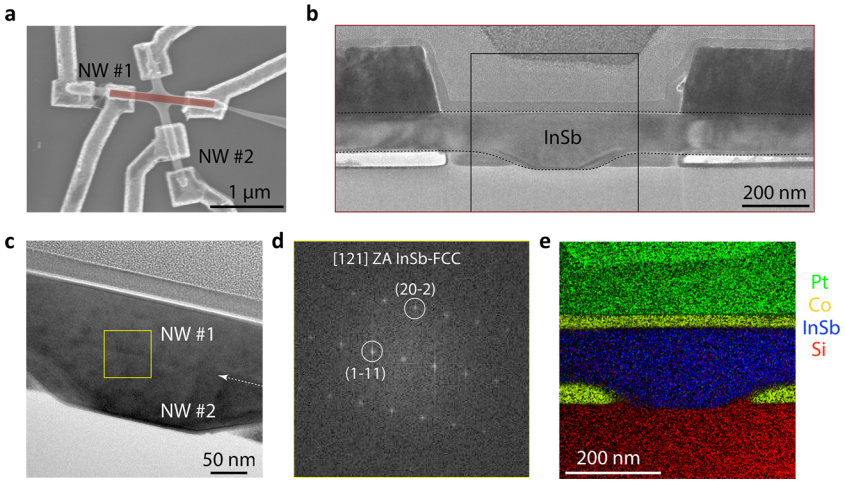

Figure 4. Structural characterization. (a) A top-view SEM image of the InSb NW network device. The red rectangle indicates a lamella of the device along one of the nanowires which was prepared using a focused ion beam to be inspected in TEM. The resulting low-magnification bright-field TEM image is shown in panel b. The intersection of the two constituent nanowires denoted as NW#1 and NW#2 is highlighted by a black square. (c) High-resolution TEM image of the junction viewed along the [121] zone axis. The white arrow indicates the sharp clean interface between the two crossed nanowires. (d) Fast Fourier transform (FFT) pattern evaluated at the interface between the two crossed nanowires indicated by a yellow square in panel c reveals the zinc blende crystalline structure of the junction. (e) EDX compositional map of the device cross section. The InSb NW network is shown in blue and Si/SiO_2 substrate in red. Layers of Pt and Co (shown in green and yellow, respectively) have been deposited during focused ion beam sample preparation to protect the junction from induced damage.

splitting ($E_{Zeeman} = g\mu_B B$). Using this approach, we estimate g_1 of 43, 43, and 52 corresponding to the subband spacing, $\Delta_{subband}$, of 21, 21, and 25 meV for the different channels A−B, A−C, and A−D, respectively. The estimated g_1 values for the different contact pairs are close to the expected InSb bulk value of 51. Data from additional devices are included in S7−10 demonstrating consistent results and ballistic transport in all three devices.

To gain more insight about the structural quality of the junction between crossed NWs in the measured NW networks, device II (its transport data is shown in S7 and S8) was sliced open using focused ion beam (FIB). A 50 nm thin lamella along one of the NWs (indicated by a red line in Figure 4a was prepared and inspected in a transmission electron microscope (TEM). Both the cross-sectional TEM images (Figure 4c) and the energy-dispersive X-ray spectroscopy (EDX) map (Figure 4e) show a sharp and oxide-free interface between the crossed NWs. Moreover, the zinc blende crystal structure of the junction is confirmed by the FFT pattern of the lattice imaged along the [121] direction as shown in Figure 4d. The high quality of the junction based on this structural analysis supports the ballistic transport behavior observed in these devices.

We have demonstrated conductance quantization between most of the contact pairs in InSb NW networks at a nonzero magnetic field, and this observation is consistent over three different devices. Bias voltage spectroscopy on these quantized plateaus at a finite magnetic field measures spin-resolved subband spacing, enabling an estimation of Landé g-factor above 40 in these NW networks. The demonstration of ballistic transport through two orthogonal channels in an InSb NW network represents a major step toward braiding of Majorana zero modes. Further improvements are expected from appropriate nanowire surface passivation[31] and the use of low-noise dielectrics.[25]

■ ASSOCIATED CONTENT

Supporting Information

The Supporting Information is available free of charge on the ACS Publications website at DOI: 10.1021/acs.nanolett.7b00797.

Supporting video (ZIP)

Detailed fabrication recipe, InSb nanowire network transfer, and additional electronic transport data of the main device as well as other devices (PDF)

■ AUTHOR INFORMATION

Corresponding Authors

*E-mail: e.p.a.m.bakkers@tue.nl.
*E-mail: H.Zhang-3@tudelft.nl.

ORCID

Elham M. T. Fadaly: 0000-0001-7074-8784
Diana Car: 0000-0002-6371-8285
Sebastian Kölling: 0000-0002-6606-9110
Erik P. A. M. Bakkers: 0000-0002-8264-6862

Present Address

S.R.P.: CNRS-Laboratoire d'Analyze et d'Architecture des Systemes (LAAS), Universitéde Toulouse, 7 avenue du Colonel Roche, F-31400 Toulouse, France.

Author Contributions

E.M.T.F. and H.Z. contributed equally.

Funding

This work has been supported by The Netherlands Organization for Scientific Research (NWO), Foundation for Fundamental Research on Matter (FOM), European Union Seventh Framework Programme, European Research Council (ERC), Office of Naval Research (ONR), and Microsoft Corporation Station Q.

Notes

The authors declare no competing financial interest.

■ ACKNOWLEDGMENTS

We thank Dr. Sergey Frolov for the very fruitful discussions and Dr. Kun Zuo, Alain Dijkstra, and Ghada Badawy for the critical reading of the manuscript.

DOI: 10.1021/acs.nanolett.7b00797
Nano Lett. 2017, 17, 6511−6515

REFERENCES

(1) Fu, L.; Kane, C. L. *Phys. Rev. Lett.* **2008**, *100* (9), 1−4.
(2) Alicea, J. *Rep. Prog. Phys.* **2012**, *75* (7), 076501.
(3) Das Sarma, S.; Freedman, M.; Nayak, C. *npj Quantum Inf.* **2015**, *1*, 15001.
(4) Lutchyn, R. M.; Sau, J. D.; Das Sarma, S. *Phys. Rev. Lett.* **2010**, *105* (7), 077001.
(5) Oreg, Y.; Refael, G.; von Oppen, F. *Phys. Rev. Lett.* **2010**, *105* (17), 177002.
(6) Mourik, V.; Zuo, K.; Frolov, S. M.; Plissard, S. R.; Bakkers, E. P. A. M.; Kouwenhoven, L. P. *Science (Washington, DC, U. S.)* **2012**, *336* (6084), 1003−1007.
(7) Das, A.; Ronen, Y.; Most, Y.; Oreg, Y.; Heiblum, M.; Shtrikman, H. *Nat. Phys.* **2012**, *8* (12), 887−895.
(8) Deng, M. T.; Yu, C. L.; Huang, G. Y.; Larsson, M.; Caroff, P.; Xu, H. Q. *Nano Lett.* **2012**, *12* (12), 6414−6419.
(9) Zhang, H.; Gül, Ö.; Conesa-Boj, S.; Zuo, K.; Mourik, V.; de Vries, F. K.; van Veen, J.; van Woerkom, D. J.; Nowak, M. P.; Wimmer, M.; Car, D.; Plissard, S.; Bakkers, E. P. A. M.; Quintero-Pérez, M.; Goswami, S.; Watanabe, K.; Taniguchi, T.; Kouwenhoven, L. P. *arXiv:1603.04069* **2016**, 1−21.
(10) Churchill, H. O. H.; Fatemi, V.; Grove-Rasmussen, K.; Deng, M. T.; Caroff, P.; Xu, H. Q.; Marcus, C. M. *Phys. Rev. B: Condens. Matter Mater. Phys.* **2013**, *87* (24), 241401.
(11) Finck, A. D. K.; Van Harlingen, D. J.; Mohseni, P. K.; Jung, K.; Li, X. *Phys. Rev. Lett.* **2013**, *110* (12), 126406.
(12) Albrecht, S. M.; Higginbotham, A. P.; Madsen, M.; Kuemmeth, F.; Jespersen, T. S.; Nygård, J.; Krogstrup, P.; Marcus, C. M. *Nature* **2016**, *531* (7593), 206−209.
(13) Chen, J.; Yu, P.; Stenger, J.; Hocevar, M.; Car, D.; Plissard, S. R.; Bakkers, E. P. A. M.; Stanescu, T. D.; Frolov, S. M. *arXiv*:1610.04555, **2016**.
(14) Deng, M. T.; Vaitiekenas, S.; Hansen, E. B.; Danon, J.; Leijnse, M.; Flensberg, K.; Nygård, J.; Krogstrup, P.; Marcus, C. M. *Science (Washington, DC, U. S.)* **2016**, *354* (6319), 1557−1562.
(15) Alicea, J. *Rep. Prog. Phys.* **2012**, *75* (7), 076501.
(16) Aasen, D.; Hell, M.; Mishmash, R. V; Higginbotham, A.; Danon, J.; Leijnse, M.; Jespersen, T. S.; Folk, J. A.; Marcus, C. M.; Flensberg, K.; Alicea, J. *Phys. Rev. X* **2016**, *6* (3), 031016.
(17) Hyart, T.; van Heck, B.; Fulga, I. C.; Burrello, M.; Akhmerov, A. R.; Beenakker, C. W. J. *Phys. Rev. B: Condens. Matter Mater. Phys.* **2013**, *88* (3), 35121.
(18) Mi, S.; Pikulin, D. I.; Wimmer, M.; Beenakker, C. W. J. *Phys. Rev. B: Condens. Matter Mater. Phys.* **2013**, *87* (24), 241405.
(19) van Heck, B.; Akhmerov, A. R.; Hassler, F.; Burrello, M.; Beenakker, C. W. J. *New J. Phys.* **2012**, *14* (3), 035019.
(20) Gül, Ö.; Woerkom, D. J.; van Weperen, I.; Car, D.; Plissard, S. R.; Bakkers, E. P. A. M.; Kouwenhoven, L. P. *Nanotechnology* **2015**, *26* (21), 215202.
(21) van Weperen, I.; Tarasinski, B.; Eeltink, D.; Pribiag, V. S.; Plissard, S. R.; Bakkers, E. P. A. M.; Kouwenhoven, L. P.; Wimmer, M. *Phys. Rev. B: Condens. Matter Mater. Phys.* **2015**, *91* (20), 201413.
(22) van den Berg, J. W. G.; Nadj-Perge, S.; Pribiag, V. S.; Plissard, S. R.; Bakkers, E. P. A. M.; Frolov, S. M.; Kouwenhoven, L. P. *Phys. Rev. Lett.* **2013**, *110* (6), 066806.
(23) Nadj-Perge, S.; Pribiag, V. S.; van den Berg, J. W. G.; Zuo, K.; Plissard, S. R.; Bakkers, E. P. A. M.; Frolov, S. M.; Kouwenhoven, L. P. *Phys. Rev. Lett.* **2012**, *108* (16), 166801.
(24) Nilsson, H. A.; Caroff, P.; Thelander, C.; Larsson, M.; Wagner, J. B.; Wernersson, L.-E.; Samuelson, L.; Xu, H. Q. *Nano Lett.* **2009**, *9* (9), 3151−3156.
(25) Kammhuber, J.; Cassidy, M. C.; Zhang, H.; Gül, Ö.; Pei, F.; de Moor, M. W. A.; Nijholt, B.; Watanabe, K.; Taniguchi, T.; Car, D.; Plissard, S. R.; Bakkers, E. P. A. M.; Kouwenhoven, L. P. *Nano Lett.* **2016**, *16* (6), 3482−3486.
(26) Car, D.; Wang, J.; Verheijen, M. A.; Bakkers, E. P. A. M.; Plissard, S. R. *Adv. Mater.* **2014**, *26* (28), 4875−4879.
(27) Plissard, S. R.; van Weperen, I.; Car, D.; Verheijen, M. A.; Immink, G. W. G.; Kammhuber, J.; Cornelissen, L. J.; Szombati, D. B.; Geresdi, A.; Frolov, S. M.; Kouwenhoven, L. P.; Bakkers, E. P. A. M. *Nat. Nanotechnol.* **2013**, *8* (11), 859−864.
(28) Kang, J. H.; Cohen, Y.; Ronen, Y.; Heiblum, M.; Buczko, R.; Kacman, P.; Popovitz-Biro, R.; Shtrikman, H. *Nano Lett.* **2013**, *13* (11), 5190−5196.
(29) Rieger, T.; Rosenbach, D.; Vakulov, D.; Heedt, S.; SchäPers, T.; Grützmacher, D.; Lepsa, M. I. *Nano Lett.* **2016**, *16* (3), 1933−1941.
(30) Heedt, S.; Vakulov, D.; Rieger, T.; Rosenbach, D.; Trellenkamp, S.; Grützmacher, D.; Lepsa, M. I.; SchäPers, T. *Adv. Electron. Mater.* **2016**, *2* (15), 1500460−1500466.
(31) Gooth, J.; Borg, M.; Schmid, H.; Schaller, V.; Wirths, S.; Moselund, K.; Luisier, M.; Karg, S.; Riel, H. *Nano Lett.* **2017**, *17* (4), 2596−2602.
(32) van Weperen, I.; Plissard, S. R.; Bakkers, E. P. A. M.; Frolov, S. M.; Kouwenhoven, L. P. *Nano Lett.* **2013**, *13* (2), 387−391.
(33) Plissard, S. R.; Slapak, D. R.; Verheijen, M. A.; Hocevar, M.; Immink, G. W. G.; Van Weperen, I.; Nadj-Perge, S.; Frolov, S. M.; Kouwenhoven, L. P.; Bakkers, E. P. A. M. *Nano Lett.* **2012**, *12* (4), 1794−1798.

DOI: 10.1021/acs.nanolett.7b00797
Nano Lett. 2017, 17, 6511−6515